Vacuum 160 (2019) 95–101

Contents lists available at ScienceDirect

Vacuum

journal homepage: www.elsevier.com/locate/vacuum

In-situ fabrication and characteristics of an $Al_4W/Al_{12}W$ composite using infiltration method

Chan Wang[a,b], Shuhua Liang[a,b,*], Yihui Jiang[a,b]

[a] School of Materials Science and Engineering, Xi'an University of Technology, Xi'an, 710048, China
[b] Shaanxi Province Key Laboratory of Electrical Materials and Infiltration Technology, Xi'an University of Technology, Xi'an, 710048, China

ARTICLE INFO

Keywords:
$Al_4W/Al_{12}W$ composites
Infiltration
Electron backscatter diffraction
First-principles calculations
Microstructural evolution

ABSTRACT

A novel $Al_4W/Al_{12}W$ composite, which can be used as a structural material in the automotive and aerospace industries, was developed and successfully fabricated in-situ using an infiltration method in vacuum environment. The microstructure and phase analyses of the $Al_4W/Al_{12}W$ composite were performed using a scanning electron microscope equipped with energy dispersive spectrum and X-ray diffractometer. To quantify the characteristics of the composite, electron backscattering diffraction analysis and first-principles calculations were then performed. The composite was obtained at 800 °C, and the Al_4W phase was distributed homogeneously on the $Al_{12}W$ with holding time above 40 min at 800 °C. The grain size of Al_4W increased, while its relative content decreased with longer holding time. The structural stability of Al_4W was superior to that of $Al_{12}W$. The microstructural evolution of $Al_4W/Al_{12}W$ composite was also elucidated. The defined microstructure promised favorable engineering applications of the novel composite.

1. Introduction

Tungsten-aluminum intermetallics combine the great strength, hardness and heat resistance of tungsten (W) with the resistance to oxidation and low density of aluminum (Al). These intermetallics are being actively examined for potential application in automotive and aerospace industries as the raw material for fabricating aircraft engines, armour plating and as anti-corrosive coatings [1–4]. A similar widely-applied material in the aerospace field is ceramic matrix composites (CMCs), which have excellent high temperature stability, corrosion resistance and great strength [5–8]. These outstanding properties are mainly achieved through the ceramic phase including WC, Al_2O_3, SiC, Si_3N_4 et al. [9–13]. These ceramic phase materials may be enhanced the tensile strength of metal matrix composites. For example, the tensile strength of an aluminum alloy was increased by 16%, when it was reinforced with WC [14]. However, the in situ $Al_{12}W$ particles were able to enhance the tensile strength of an aluminum matrix composite by 84.5% [15], which indicates that $Al_{12}W$ can be comparable to traditional ceramic phase materials in the ability to produce composites with achieve extraordinary properties. $Al_{12}W$ with exotic high strength is due to the covalent strengthening produced by the introduction of the extra-electron, which dramatically transforms the metal bond into a covalent bond by changing the critical valence electron concentration [16]. Another kind of tungsten-aluminum intermetallic, Al_4W shows great high temperature stability [17]. Therefore, it is advantageous to develop an $Al_4W/Al_{12}W$ composite in order to fabricate a material with both high strength and temperature stability.

However, there was no existing method for preparing an $Al_4W/Al_{12}W$ composite. CMCs can be fabricated by many techniques, such as powder metallurgy (PM) and sintering process [18–20], polymer infiltration pyrolysis (PIP) [21,22], self-propagating high-temperature synthesis (SHS) [23,24], and chemical vapor deposition (CVD) [25,26]. However, due to the large discrepancy in density, melting point and coefficient of thermal expansion between W and Al, it has been difficult to prepare the desired $Al_4W/Al_{12}W$ composite. In this study, an infiltration method was developed since it can produce large structural components with complex geometry economically and easily. The $Al_4W/Al_{12}W$ composite was created by the infiltration of a pre-sintered tungsten skeleton with molten aluminum. The microstructure of $Al_4W/Al_{12}W$ composite was then characterized by several techniques. The first-principles calculation was made to determine the stability of the Al_4W and $Al_{12}W$. Experimental and computational analyses were performed to characterize the Al_4W and $Al_{12}W$. These characteristics and the microstructural evolution of the $Al_4W/Al_{12}W$ composite are elaborated in detail in this paper. This research enhances the understanding of the formation mechanism and the characteristics of this $Al_4W/Al_{12}W$ composite, and establishes the foundation for future applications of this new material in the aeronautical industry. Also, this

* Corresponding author. School of Materials Science and Engineering, Xi'an University of Technology, Xi'an, 710048, China.
E-mail address: liangsh@xaut.edu.cn (S. Liang).

https://doi.org/10.1016/j.vacuum.2018.11.018
Received 14 September 2018; Received in revised form 9 November 2018; Accepted 9 November 2018
Available online 12 November 2018
0042-207X/

work provides a guide for the related research and development of Al-W-X (X = Co, Ni, Cu) composites.

2. Materials and methods

2.1. Preparation and characterization

The raw materials, aluminum ingot (purity ≥ 99.9 wt%) and tungsten powders (purity ≥ 99.9 wt%, average particle size of 6–8 μm), were prepared initially for the fabrication of the $Al_4W/Al_{12}W$ composites. The pre-sintered tungsten skeletons were produced by pressure applied to the tungsten powders in a hydraulic machine to form tungsten green bodies (density = 60%), followed by heating the tungsten bodies at 1000 °C for 40 min in a furnace with atmospheric protection. Hydrogen (H_2) was used as the atmospheric protection in the initial heating-up and heat-preservation stage, and nitrogen (N_2) was used for protection in the cooling stage. Afterwards, the sintered tungsten skeletons were infiltrated with molten aluminum at 800 °C in a vacuum furnace with a vacuum of 2.3–4.5 × 10^{-3} Pa. The temperature precision of the sintering furnace is ± 5 °C. The infiltrates were then held at temperature for different time (10 min, 40 min, 50 min and 60 min) and the reaction process between aluminum and tungsten was observed step by step. After the furnace cooling down, the $Al_4W/Al_{12}W$ composites were obtained. The achieved composites were machined and polished for later characterization. A microstructural observation was carried out using a JEOL JSM-6700F field-emission scanning electron microscope (FESEM). The phase and grain distribution of the composite were visualized by electron backscattering diffraction (EBSD) on a Zeiss-Merlin SEM, with an acceleration voltage of 20 kV. The X-ray diffraction patterns were generated by an XRD-7000S X-ray diffractometer with Cu *Kα* radiation.

2.2. Computational details

The present calculations were based on the plane-wave pseudopotential density functional theory (DFT) implemented in the Cambridge Serial Total Energy Package (CASTEP) code [27–29]. The Perdew-Burke-Ernzerhof (PBE) functional version of the generalized gradient approximation (GGA) was used as exchange-correlation functional [30]. The Kohn-Sham equation was solved by means of the ultrasoft pseudopotentials introduce by Vanderbilt [31]. Pseudo-atomic calculations were performed for Al $3s^2 3p^1$ and W $5p^6 d^4 6s^2$, respectively. The plane wave cut-off energy of 350 eV was employed for Al_4W and $Al_{12}W$. For Brillouin zone sampling, a 5 × 5 × 5 Monkhorst-Pack [32] mesh was adopted for Al_4W and an 11 × 11 × 11 Monkhorst-Pack mesh for $Al_{12}W$. Geometric optimization of the structures was performed within the Broyden-Fletcher-Goldfarb-Shanno (BFGS) minimization scheme [33], with the following thresholds for converged structures: energy change per atom, maximum residual force, maximum atomic displacement and maximum stress were less than 5 × 10^{-6} eV, 0.01 eV/Å, 5 × 10^{-4} Å and 0.02 GPa respectively.

3. Results

3.1. Morphologies and phase analysis

The cross-sectional morphology of the Al/W diffusion couple synthesized at 800 °C for 10 min showed a wavy transition zone with thickness of ~500 μm formed at the Al/W interface (Fig. 1(a)). A wide depth of penetration was obtained, indicating a good infiltration of the tungsten matrix by the aluminum. Moreover, colour-contrastive zones (light and dark grey), different from the matrix were also observed, suggesting that Al-W intermetallic phases were formed at the interface. The EDS line-scan displayed the distribution of Al and W atoms across the interface, demonstrating that atomic diffusion did occur, and that Al easily diffused into the W skeletons, during the infiltration process (Fig. 1(b)). Closer observation of the interface at higher magnification (Fig. 1(c)) showed that the W particles at the interface were much smaller than the original W particles. The EDS scans were performed on both A and B regions, as shown in Fig. 1(c), and the weight-percent of W and Al were illustrated in Fig. 1(d). Comparing the weight-percent with the W-Al binary diagram [34], the newly generated A and B phases may be preliminarily considered to be Al_4W and $Al_{12}W$.

When the holding time was extended to 40 min, 50 min and 60 min, a uniform and dense $Al_4W/Al_{12}W$ microstructure was formed (Fig. 2). It is important to note that the diffusion interface disappeared completely, and no tungsten or aluminum matrix was found in the diffusion zone compared to the composite fabricated with a holding time of 10 min. Large amounts of the A phase were homogeneously distributed on the B phase, and the A phase was significantly larger than B phase. It was inferred that an adequate in-situ reaction occurred between tungsten and the aluminum matrix, allowing the A phase to continuously grow by interconnections with each other as the holding time was prolonged.

The A and B phases were further identified by XRD analysis (Fig. 3). In Fig. 3(a), it can be seen that the main phases are W and Al along with some Al_4W at a holding time of 10 min. The diffraction peaks of $Al_{12}W$ phase were not observed. However, by increasing the holding time to 40 min, Al_4W and $Al_{12}W$ were generated in large quantities as the major phases, and the intensity of the Al_4W phase was much greater than $Al_{12}W$, see Fig. 3(b). Consequently, it was believed that the A and B phases were Al_4W and $Al_{12}W$. The results of XRD analysis matched the conclusions obtained from the EDS analysis.

3.2. EBSD characterization of $Al_4W/Al_{12}W$ composites

EBSD analysis of the $Al_4W/Al_{12}W$ composites was carried out to quantify the phase constituents, grain size variation and distribution. The EBSP function during EBSD exposure was introduced to identify the crystallographic structure of each phase, which corresponded to the phase constituents of $Al_4W/Al_{12}W$ composites, as shown in Fig. 4(a), (b) and (c). The composite consisted mainly of Al_4W and $Al_{12}W$ with a few Al and W residues, which means that the entirely in-situ reaction occurred when the holding time was above 40 min. To determine the grain size variation of the Al_4W and $Al_{12}W$ phases, the Euler angle orientation and the grain size distribution of the $Al_4W/Al_{12}W$ composite were measured (Fig. 4(d-f) and 4(g-i)). The misorientation distribution for both Al_4W and $Al_{12}W$ was revealed to be more localized within the low-angle range. When holding time was increased from 40 min to 60 min, it was observed that the average grain size of Al_4W increased from 1.35 μm (40 min) to 2.31 μm (60 min), while the grain size of $Al_{12}W$ slightly increased from 1.16 μm (40 min) to 1.51 μm (60 min); the degree variation of grain size for Al_4W and $Al_{12}W$ was 71.11% and 30.17%, which can be attributed to the fact that longer holding time enhances atomic diffusion, promotes the migration rate of the grain boundary, and thus increase the grain size (Fig. 4(g-i)).

The relative content of the Al_4W phase was larger than that of $Al_{12}W$ phase (Fig. 5). The relative content of the Al_4W phase decreased as the holding time increased; however, the $Al_{12}W$ phase presented the opposite trend. The relative content of Al_4W decreased from 78.2% (40 min) to 62.3% (60 min), while the relative content of $Al_{12}W$ increased from 20% (40 min) to 35.7% (60 min). As a result, the remaining initial content of Al and W was around 2%. The results were consistence with previous SEM and XRD results.

3.3. First-principles calculation of Al_4W and $Al_{12}W$

The characterization results revealed that the desirable $Al_4W/Al_{12}W$ composite was obtained by increasing the holding time to 40 min, where Al_4W and $Al_{12}W$ were the major phases. For better understanding of the formation mechanism of the composite, the structural stability and formation sequence of the intermetallics were analyzed. The formation enthalpy (ΔH) and cohesive energy (ΔE) of the

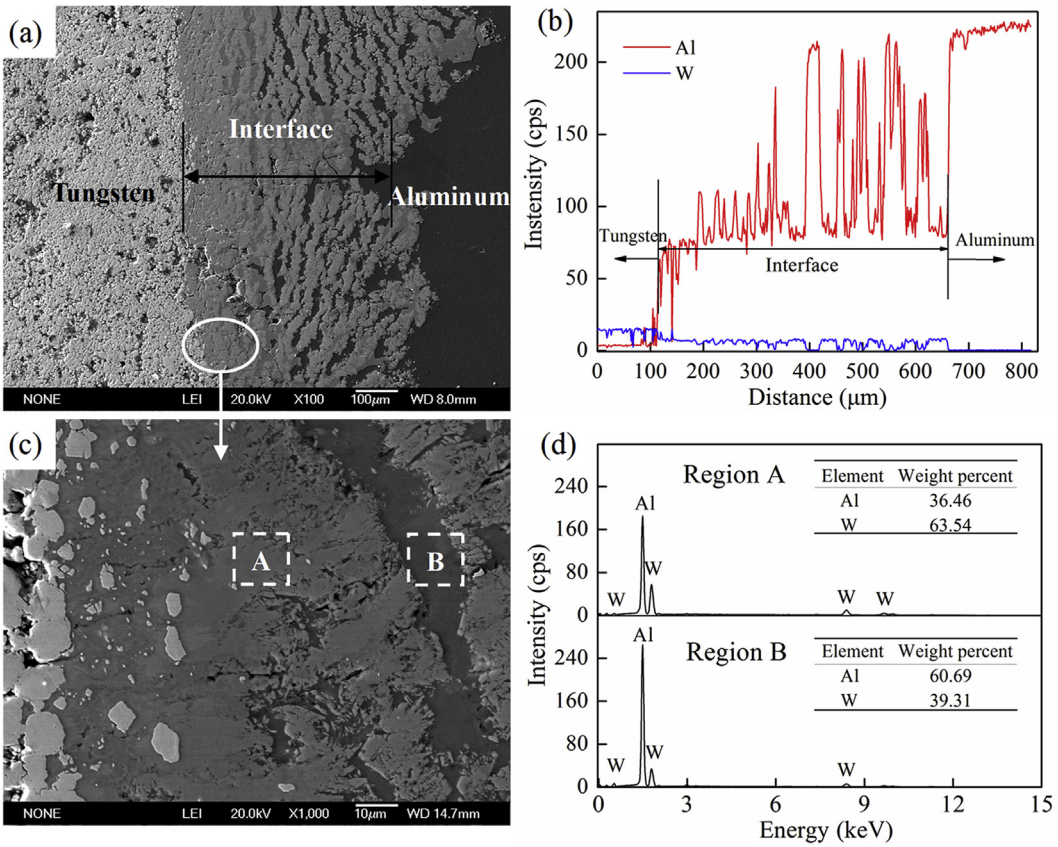

Fig. 1. (a) SEM micrograph of $Al_4W/Al_{12}W$ composite synthesized at 800 °C for 10 min; (b) EDS results of line-scan at W/Al interface. Red line represents aluminum, blue line represents tungsten; (c) enlarged images of white ellipse areas in Fig. 1a; (d) EDS results of region A and B. The weight percentage of W and Al are shown in the inset. (For interpretation of the references to colour in this figure legend, the reader is referred to the Web version of this article.)

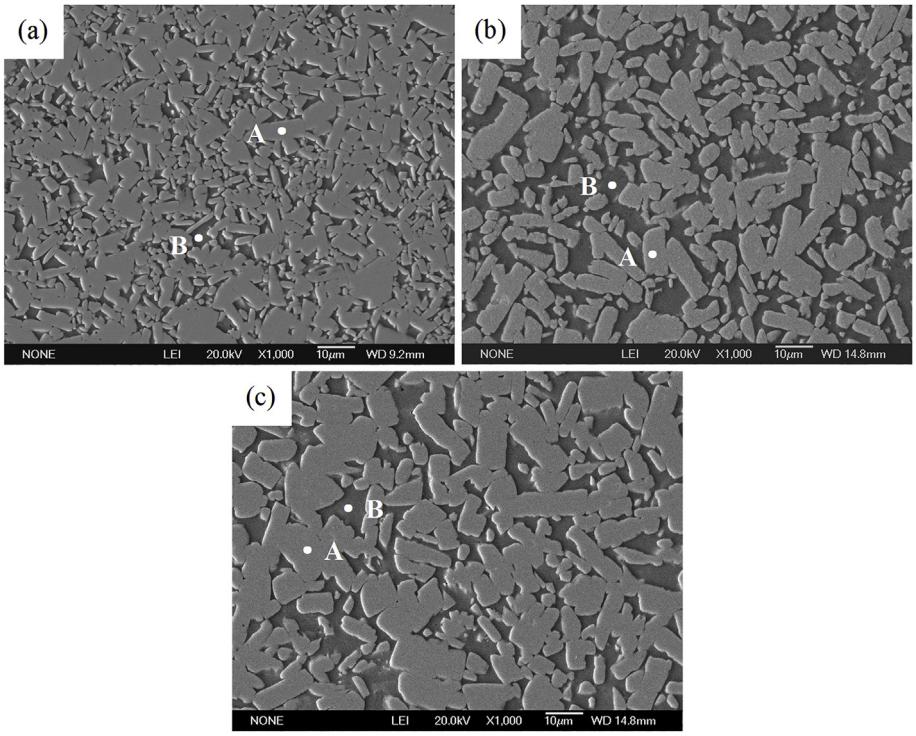

Fig. 2. Morphologies of $Al_4W/Al_{12}W$ composite synthesized at 800 °C for 40 min (a), 50 min (b) and 60 min (c) at different magnifications. A and B represents different phase.

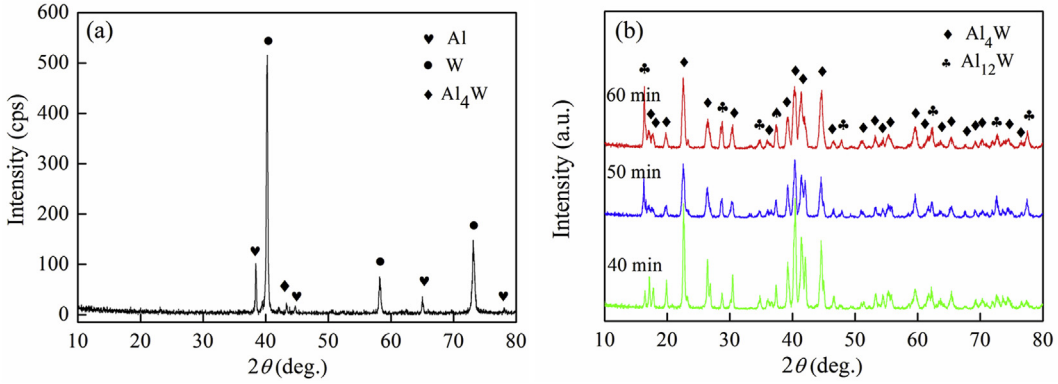

Fig. 3. XRD patterns of $Al_4W/Al_{12}W$ composite synthesized at 800 °C with different holding time: (a) 10 min, (b) 40 min, 50 min and 60 min.

intermetallics were obtained based on first-principles calculations. The primitive cell was used for all calculations. The ΔE and ΔH were calculated by Eqs. (1) and (2) [35],

$$\Delta E(Al_mW_n) = \frac{[E_{total}(Al_mW_n) - mE_{atom}(Al) - nE_{atom}(W)]}{m+n} \quad (1)$$

$$\Delta H(Al_mW_n) = \frac{[E_{total}(Al_mW_n) - mE_{solid}(Al) - nE_{solid}(W)]}{m+n} \quad (2)$$

where E_{total} (Al_mW_n), $E_{atom}(X)$ and $E_{solid}(X)$ are the total energies of the intermetallics at equilibrium lattice constant, isolated atomic energy and solid atomic energy of the pure constituents. The face centered cubic (*fcc*) structure for Al and the body centered cubic (*bcc*) structure for W were chosen as be their most stable states. The isolated atomic energies were calculated using a cubic crystal with a lattice constant of 10 Å.

The calculated results are given in Table 1. They show that the formation enthalpy of Al_4W phase (−0.1789 eV/atom) was lower than that of $Al_{12}W$ (−0.1114 eV/atom), implying that Al_4W had a stronger alloying ability than $Al_{12}W$. This is consistent with the result in Ref. [36]. The cohesive energy of Al_4W (−5.4643 eV/atom) was less than that of the $Al_{12}W$ (−4.4347 eV/atom), demonstrating that Al_4W outperformed $Al_{12}W$ in structural stability. It was hypothesized that Al_4W

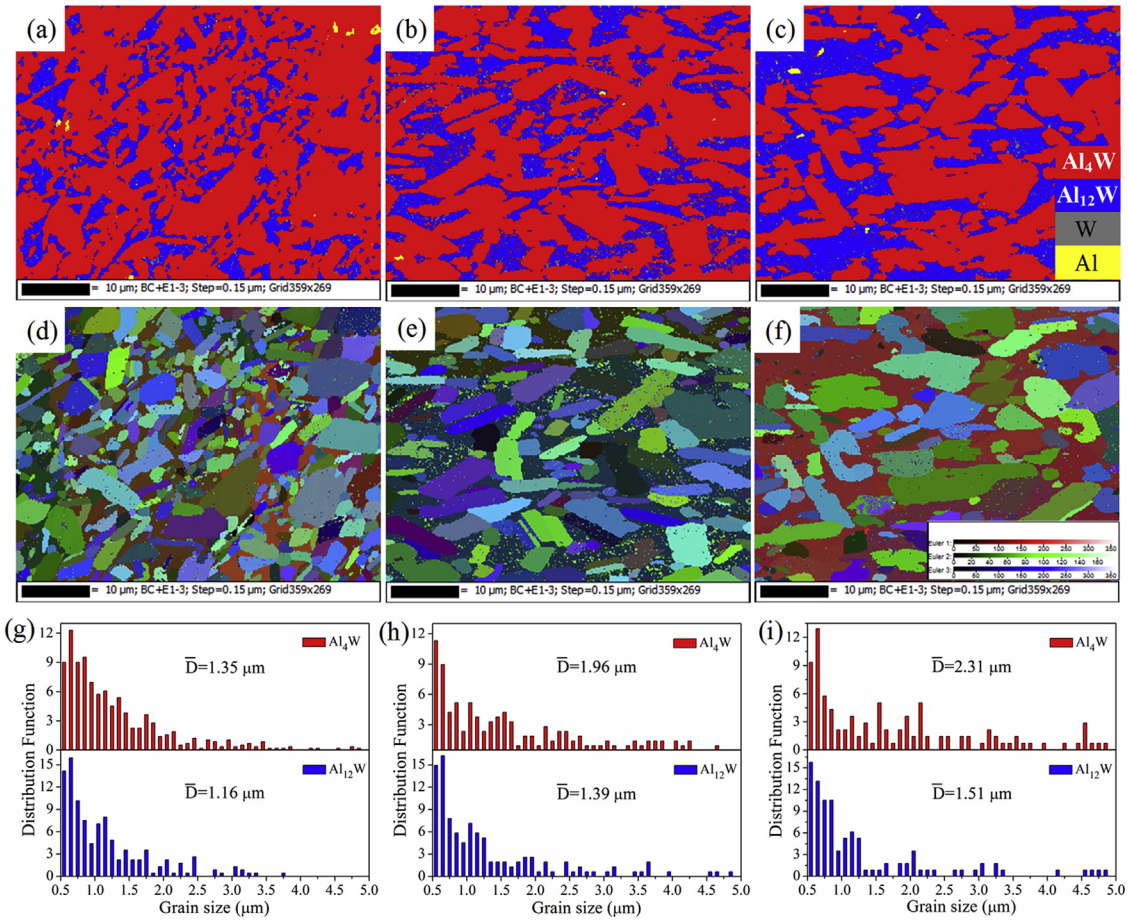

Fig. 4. EBSD results of $Al_4W/Al_{12}W$ composite synthesized at 800 °C for 40 min, 50 min and 60 min; (a, b, c) are phase distribution, (red: Al_4W, blue: $Al_{12}W$, gray: W and yellow: Al); (d, e, f) are Euler angle orientation (colors correspond to different angles); (g, h, i) are grain size distribution of Al_4W and $Al_{12}W$ (red: Al_4W, blue: $Al_{12}W$). (For interpretation of the references to colour in this figure legend, the reader is referred to the Web version of this article.)

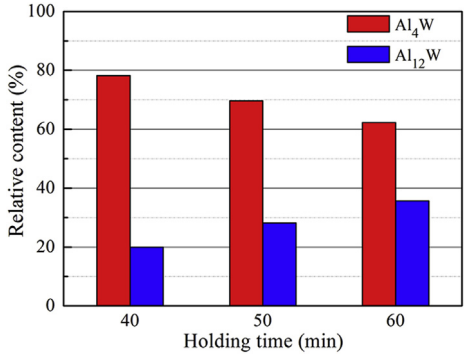

Fig. 5. Relative content of Al_4W and $Al_{12}W$ phases for the $Al_4W/Al_{12}W$ composite synthesized at 800 °C holding for different time (red: Al_4W, blue: $Al_{12}W$). (For interpretation of the references to colour in this figure legend, the reader is referred to the Web version of this article.)

Table 1
Calculation of formation enthalpy ΔH and cohesive energy ΔE of intermetallic compounds.

Intermetallic compounds	Formation enthalpy (eV/atom)	Cohesive energy (eV/atom)
Al_4W	−0.1789	−5.4643
$Al_{12}W$	−0.1114	−4.4347

was generated first followed by $Al_{12}W$ during the formation of the $Al_4W/Al_{12}W$ composite. However, Van G [37] and Krafcsik [38] have reported that $Al_{12}W$ was formed first in the W/Al interface reaction at a temperature of about 500 °C through the film method. The disagreement between our results and their findings is most likely due to the different diffusion kinetics and mechanisms caused by the different reaction temperatures.

4. Discussion

4.1. The stability of Al_4W and $Al_{12}W$

To elucidate the bonding characteristics of Al_4W and $Al_{12}W$ and better understand their structural stabilities, the total density of state (TDOS) and partial density of state (PDOS) of Al_4W and $Al_{12}W$ were calculated, shown in Fig. 6. It is clear that the bonding states of Al_4W and $Al_{12}W$ are, in general, consistent and that the Fermi level resides at the left side of the pseudogap valley, i.e. the bonding states are incompletely occupied. In addition, the main bonding states between −10 eV and −3 eV are predominantly derived from Al-3s states, and the main bonding states between −3 eV and 0 eV are dominated by Al-3p and W-5d. There is a strong hybridization derived from the Al 3s, 3p-orbitals and W 5d-orbital below the Fermi level, indicating that a strong covalent bonding exists between Al and W atoms. That is the main reason why Al_4W has a maximum negative formation enthalpy and good structural stability.

Generally, the n (E_f) is positively correlated with the stability of the phase [39]. The TDOS of Al_4W and $Al_{12}W$ were generally similar, but they were different at the Fermi level. Al_4W had a smaller n (E_f) of 0.261 states/eV/atom, while $Al_{12}W$ had 0.318 states/eV/atom. Consequently, the Al_4W phase was more stable than $Al_{12}W$.

4.2. The grain size and relative content of Al_4W

It is interesting that the average grain size of Al_4W increased from 1.35 μm to 2.31 μm, while the relative content of Al_4W decreased from 78.2% to 62.3% with increased holding time, as shown in Figs. 4 and 5. Based on the first principles calculations and the experimental observation of intermetallics, we propose that Al_4W was generated first followed by $Al_{12}W$. The absence of other Al-W intermetallics is possibly due to the unique chemical composition and kinetics of the process (cooling rates) [40]. These parameters play an important role in evolution of the intermetallics during the solidification of composites. This unusual variation of Al_4W may be explained as follows: as verified by experimental characterization, two main phases formed, Al_4W first and then $Al_{12}W$; during the process, a phase-transformation arose and caused a decrease in the relative content of Al_4W and coarsening of the grain boundaries of Al_4W with longer holding time [41].

4.3. The forming mechanism of $Al_4W/Al_{12}W$ composite

The microstructural evolution of the $Al_4W/Al_{12}W$ composite is depicted in Fig. 7. At the initial stage, a point-contact existed between tungsten and the aluminum matrix. As the temperature was increased, the contact area increased since the Al matrix has a low melting point (660 °C) and was easily melted. At regions with plenty of defects, Al atoms will be activated at first and then diffuse into the W matrix. An interface formed between the tungsten and aluminum matrix, and tungsten particle size gradually decreased from tungsten side to aluminum side (Fig. 1). As a result, an adsorption layer of molten aluminum was generated around the tungsten particles driven by gravity and capillary force (Fig. 7(a)). Consequently, a large amount of liquid Al flowed into the W matrix through micro-channels and covered the W particles. When the concentration of Al exceeded its solid solubility in W, Al_4W formed first because of the low formation enthalpy (Fig. 7(b)).

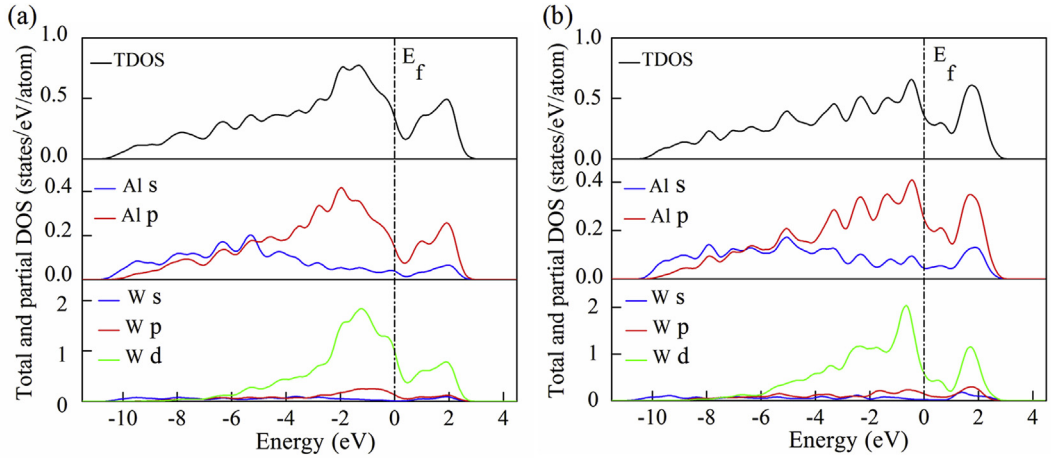

Fig. 6. Total and partial density of states for intermetallics: (a) Al_4W and (b) $Al_{12}W$. The dash-dotted lines represent the Fermi level.

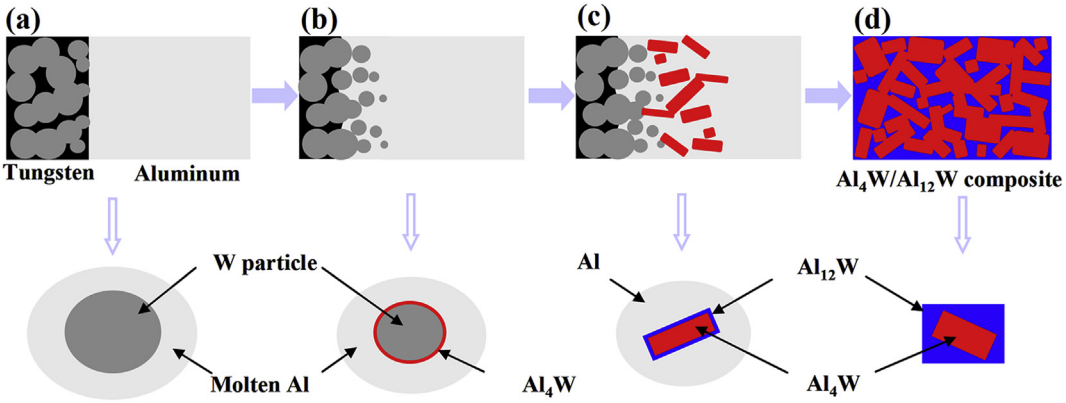

Fig. 7. Schematic illustration of the microstructural evolution used as $Al_4W/Al_{12}W$ composite.

Due to the high melting point of W, the temperature of the W particles kept rising until melting. Then the high heat was transferred to the Al matrix, promoting the diffusion of Al atom and enhancing the Al concentration around the W particle, and thus $Al_{12}W$ was gradually formed (Fig. 7(c)). With the accumulation of Al_4W around W particles, the integrants of Al_4W fall into the molten Al and continuously react with it to form $Al_{12}W$. With the prolonged holding time, the number of W and Al atoms decreased greatly, while the amount of Al_4W and $Al_{12}W$ increased sharply. $Al_{12}W$ formed at 697 °C, and the residual molten aluminum finally solidified below 660 °C. An $Al_4W/Al_{12}W$ composite, with Al_4W uniformly distributed on $Al_{12}W$, is obtained (Fig. 7(d)). The total content of Al_4W and $Al_{12}W$ reached 98% (Fig. 5), which is attributed to that the fact the tungsten matrix has high porosity and provides sufficient contact surface for the in-situ reaction with molten aluminum which has a high diffusion coefficient [42].

5. Conclusions

In summary, novel $Al_4W/Al_{12}W$ composites with uniform distribution of Al_4W on $Al_{12}W$ have been fabricated successfully by the infiltration of a pre-sintered tungsten skeleton with molten aluminum. The main findings of this work are that SEM, XRD and EBSD techniques confirmed that an entirely in-situ reaction occurred when the holding time was above 40 min. The grain size of Al_4W and $Al_{12}W$ increased with increasing holding time. Characterization analyses and calculation results consistently indicated that Al_4W formed first because of the low formation enthalpy. Further calculation disclosed that the low formation enthalpy was attributed to the fact that Al_4W has a smaller n (E_f) than $Al_{12}W$. The average grain size of Al_4W increased from 1.35 μm to 2.31 μm, while its relative content decreased from 78.2% to 62.3% with elongation of holding time. The microstructural evolution of $Al_4W/Al_{12}W$ composite was clarified that Al was the dominant diffuser.

Acknowledgment

The authors would like to acknowledge the financial support of the National Natural Science Foundation of China (No. 51371139 and U1502274), 863 Program (No. 2015AA034304), the Science and Technique Innovation Program of Shaanxi Province (No. 2012KTQ01-14), the Pivot Innovation Team of Shaanxi Electric Materials and the Infiltration Technique (No. 2012KCT-25) and Shaanxi Provincial Project of Special Foundation of Key Disciplines for this research.

References

[1] C. Ren, Z.Z. Fang, M. Koopman, B. Butler, J. Paramore, S. Middlemas, Methods for improving ductility of tungsten - a review, Int. J. Refract. Metals Hard Mater. 75 (2018) 170–183.
[2] O.B. Malyshev, A.P. Smith, R. Valizadeh, A. Hannah, Electron stimulated desorption from aluminium alloy and aluminium coated stainless steel, Vacuum 85 (2011) 1063–1066.
[3] C.L. Zhang, P. Lv, J. Cai, Y.W. Zhang, H. Xia, Q.F. Guan, Enhanced corrosion property of W-Al coatings fabricated on aluminum using surface alloying under high-current pulsed electron beam, J. Alloy. Comp. 723 (2017) 258–265.
[4] R. Winiczenko, O. Goroch, A. Krzyńska, M. Kaczorowski, Friction welding of tungsten heavy alloy with aluminum alloy, J. Mater. Process. Technol. 246 (2017) 42–55.
[5] R.S. Kumar, Crack-growth resistance behavior of mode-I delamination in ceramic matrix composites, Acta Mater. 131 (2017) 511–522.
[6] H. Ohnabe, S. Masaki, M. Onozuka, K. Miyahara, T. Sasa, Potential application of ceramic matrix composites to aero-engine components, Compos. Appl. Sci. Manuf. 30 (1999) 489–496.
[7] C. Ferraro, S. Meille, J. Réthoré, N. Ni, J. Chevalier, E. Saiz, Strong and tough metal/ceramic micro-laminates, Acta Mater. 144 (2018) 202–215.
[8] S. Poges, C. Monteleone, K. Petroski, G. Richards, S.L. Suib, Preparation and characterization of an oxide-oxide continuous fiber reinforced ceramic matrix composite with a zinc oxide interphase, Ceram. Int. 43 (2017) 17121–17127.
[9] Y.G. Shi, W.G. Chen, L.L. Dong, H.Y. Li, Y.Q. Fu, Enhancing copper infiltration into alumina using spark plasma sintering to achieve high performance Al_2O_3/Cu composites, Ceram. Int. 44 (2018) 57–64.
[10] Y.S. Yi, R.F. Li, Z.Y. Xie, Y. Meng, S. Sugiyama, Effects of reheating temperature and isothermal holding time on the morphology and thixo-formability of SiC particles reinforced AZ91 magnesium matrix composite, Vacuum 154 (2018) 177–185.
[11] Y. Sahin, Preparation and some properties of SiC particle reinforced aluminium alloy composites, Mater. Des. 24 (2003) 671–679.
[12] C.C. Ye, X.Y. Yue, Y. Jiang, H.J. Li, H.Q. Ru, Effect of different preparation methods on the microstructure and mechanical properties of Si_3N_4 ceramic composites, Ceram. Int. 44 (2018) 3664–3671.
[13] Y.X. Zhao, X.G. Song, C.W. Tan, S.P. Hu, J. Cao, J.C. Feng, Microstructural evolution of Si_3N_4/Ti6Al4V joints brazed with nano-Si_3N_4 reinforced AgCuTi composite filler, Vacuum 142 (2017) 58–65.
[14] K. Ravikumar, K. Kiran, V.S. Sreebalaji, Characterization of mechanical properties of aluminium/tungsten carbide composites, Measurement 102 (2017) 142–149.
[15] Y.C. Feng, L. Geng, A.B. Li, Z.Z. Zheng, Fabrication and characteristics of in situ $Al_{12}W$ particles reinforced aluminum matrix composites by reaction sintering, Mater. Des. 31 (2010) 965–967.
[16] H.Y. Niu, X.Q. Chen, P.T. Liu, W.W. Xing, X.Y. Cheng, D.Z. Li, Y.Y. Li, Extra-electron induced covalent strengthening and generalization of intrinsic ductile-to-brittle criterion, Sci. Rep. 2 (2012) 1–6.
[17] H.G. Tang, X.F. Ma, W. Zhao, X.W. Yan, R.J. Hong, Preparation of W-Al alloys by mechanical alloying, J. Alloy. Comp. 347 (2002) 228–230.
[18] C.A. Vogiatzis, S.M. Skolianos, On the sintering mechanisms and microstructure of aluminium-ceramic cenospheres syntactic foams produced by powder metallurgy route, Compos. Part A 82 (2016) 8–19.
[19] P. Tatarko, V. Casalegno, C.F. Hu, M. Salvo, M. Ferraris, M.J. Reece, Joining of CVD-SiC coated and uncoated fibre reinforced ceramic matrix composites with pre-sintered Ti_3SiC_2 MAX phase using Spark Plasma Sintering, J. Eur. Ceram. Soc. 36 (2016) 3957–3967.
[20] H. Sheikh, M.R. Loghman-Estarki, E. Mohammad Sharifi, A. Alhaji, J. Shakeri, Toughening of $MgAl_2O_4$ spinel/Si_3N_4 nanocomposite fabricated by spark plasma sintering, Ceram. Int. 44 (2018) 18235–18242.
[21] X.H. Yang, K.Z. Li, L.T. Bai, Z.G. Zhao, Y. Wang, Thermal ablation behavior of SiC coating for 3D braided carbon fiber reinforced ZrC-SiC composites in different heat fluxes, Vacuum 156 (2018) 334–344.
[22] D. Li, B. Li, Y.Y. Zheng, S.T. Gao, X.J. Yang, On the mechanical, thermophysical and dielectric properties of Nextel^{TM} 440 fiber reinforced nitride matrix (N440/Nitride) composites, Ceram. Int. 44 (2018) 6137–6143.
[23] S. Vorotilo, E.A. Levashov, V.V. Kurbatkina, D.Y. Kovalev, N.A. Kochetov, Self-propagating high-temperature synthesis of nanocomposite ceramics $TaSi_2$-SiC with hierarchical structure and superior properties, J. Eur. Ceram. Soc. 38 (2018) 433–443.
[24] X.H. Hou, J.K. Yu, M.K. Sheng, Study on the preparation of the ceramic composite-

lined steel pipe with the SHS reaction system of Al-Fe_2O_3-Cr_2O_3, Ceram. Int. 43 (2017) 11078–11082.
[25] J. Lin, Y.H. Yang, H.A. Zhang, Q. Lin, B. Zhu, Synthesis and characterization of in-situ CNTs reinforced TiB_2-based composite by CVD using Ni catalysts, Ceram. Int. 44 (2018) 2042–2047.
[26] J.C. Ren, Y.L. Zhang, J.H. Li, S. Tian, T. Fei, H.J. Li, Effects of deposition temperature and time on HfC nanowires synthesized by CVD on SiC-coated C/C composites, Ceram. Int. 42 (2016) 5623–5628.
[27] H. L Liu, X. Zhang, Y.X. Xiao, J. Zhang, The electronic structure and thermionic emission property of single crystal SmB_6, Vacuum 145 (2017) 295–298.
[28] M. Piasecki, M.G. Brik, I.E. Barchiy, K. Ozga, I.V. Kityk, A.M. EI-Naggar, A.A. Albassam, T.A. Malakhovskaya, G. Lakshminarayana, Band structure, electronic and optical features of Tl_4SnX_3 (X = S, Te) ternary compounds for optoelectronic applications, J. Alloy. Comp. 710 (2017) 600–607.
[29] M.I. Kholil, M.S. Ali, M. Aftabuzzaman, Structural, elastic, electronic and vibrational properties of $BaRh_2P_2$ and $SrIr_2As_2$ superconductors: a DFT study, J. Alloy. Comp. 740 (2018) 754–765.
[30] J.P. Perdew, K. Burke, M. Ernzerhof, Generalized gradient approximation made simple, Phys. Rev. Lett. 77 (1996) 3865–3868.
[31] D. Vanderbilt, Soft self-consistent pseudopotentials in a generalized eigenvalue formalism, Phys. Rev. B 41 (1990) 7892–7895.
[32] H.J. Monkhorst, J.D. Pack, Special points for Brillouin-zonde integrations, Phys. Rev. B 13 (1976) 5188–5192.
[33] B.G. Pfrommer, M. Côté, S.G. Louie, M.L. Cohen, Relaxation of crystals with the Quasi-Newton method, Comput. Phys. 131 (1997) 233–240.
[34] T.B. Massalski, H. Okamoto, P.R. Subramanian, L. Kacprzak (Eds.), Binary Alloy Phase Diagrams, ASM International, Materials Park, OH, USA, 1990, pp. 198–204.
[35] C.Y. Zhao, X.Y. Wang, First-principles study of the structural, electronic, and thermodynamic properties of Rh_3Sc compound under high pressure, J. Alloy. Comp. 704 (2017) 484–490.
[36] R.S. Rajamure, H.D. Vora, S.G. Srinivasan, N.B. Dahotre, Laser alloyed Al-W coating on aluminum for enhanced corrosion resistance, Appl. Surf. Sci. 328 (2015) 205–214.
[37] G.J. van Gurp, J.L.C. Daams, A. van Oostrom, L.J.M. Augustus, Y. Tamminga, Aluminum-silicide reactions. I. Diffusion, compound formation, and microstructure, J. Appl. Phys. 50 (1979) 6915–6922.
[38] I. Krafcsik, J. Gyulai, C.J. Plamström, J.W. Mayer, Influence of Cu as an impurity in Al/Ti and Al/W thin film reactions, Appl. Phys. Lett. 43 (1983) 1015–1017.
[39] X.M. Tao, Y.Z. Liu, R.C. Wang, Y.F. Ouyang, Y. Du, Y.H. He, First-principles investigations of elastic, electronic and thermodynamic properties of $Al_{12}X$ (X = Mo, W and Re), Intermetallics 24 (2012) 15–21.
[40] Z.Y. Ding, Q.D. Hu, W.Q. Lu, X. Ge, S. Cao, S.Y. Sun, T.X. Yang, M.X. Xia, J.G. Li, Microstructural evolution and growth behavior of intermetallic compounds at the liquid Al/solid Fe interface by synchrotron X-ray radiography, Mater. Char. 136 (2018) 157–164.
[41] W. Chen, Z.S. You, N.R. Tao, Z.H. Jin, L. Liu, Mechanically-induced grain coarsening in gradient nano-grained copper, Acta Mater. 125 (2017) 255–264.
[42] R. Khoshhal, M. Soltanieh, M. Mirjalili, Formation and growth of titanium aluminide layer at the surface of titanium sheets immerged in molten aluminum, Iranian J. Mater. Sci. Eng. 7 (2010) 24–31.